Band Structure Perfection and Superconductivity in Type-II Dirac Semimetal $Ir_{1-x}Pt_xTe_2$

Fucong Fei, Xiangyan Bo, Pengdong Wang, Jianghua Ying, Jian Li, Ke Chen, Qing Dai, Bo Chen, Zhe Sun, Minhao Zhang, Fanming Qu, Yi Zhang, Qianghua Wang, Xuefeng Wang, Lu Cao, Haijun Bu, Fengqi Song, Xiangang Wan,* and Baigeng Wang**

The discovery of a new type-II Dirac semimetal in $Ir_{1-x}Pt_xTe_2$ with optimized band structure is described. Pt dopants protect the crystal structure holding the Dirac cones and tune the Fermi level close to the Dirac point. The type-II Dirac dispersion in $Ir_{1-x}Pt_xTe_2$ is confirmed by angle-resolved photoemission spectroscopy and first-principles calculations. Superconductivity is also observed and persists when the Fermi level aligns with the Dirac points. $Ir_{1-x}Pt_xTe_2$ is an ideal platform for further studies on the exotic properties and potential applications of type-II DSMs, and opens up a new route for the investigation of the possible topological superconductivity and Majorana physics.

Dr. F. C. Fei, X. Y. Bo, B. Chen, Prof. Y. Zhang, Prof. Q. H. Wang, Dr. L. Cao, Dr. H. J. Bu, Prof. F. Q. Song, Prof. X. G. Wan, Prof. B. G. Wang
National Laboratory of Solid State Microstructures
Collaborative Innovation Center of Advanced Microstructures
Department of Physics
Nanjing University
Nanjing 210093, China
E-mail: songfengqi@nju.edu.cn; xgwan@nju.edu.cn; bgwang@nju.edu.cn

P. D. Wang, Prof. Z. Sun
National Synchrotron Radiation Laboratory
University of Science and Technology of China
Hefei 230029, China

J. H. Ying, Prof. F. M. Qu
Beijing National Laboratory for Condensed Matter Physics
Institute of Physics
Chinese Academy of Sciences
Beijing 100190, China

Prof. J. Li
Westlake Institute for Advanced Study
Hangzhou 310012, China

K. Chen, Prof. Q. Dai
Nanophotonics Research Division
CAS Center for Excellence in Nanoscience
National Center for Nanoscience and Technology
Beijing 100190, China

Dr. M. H. Zhang, Prof. X. F. Wang
National Laboratory of Solid State Microstructures
Collaborative Innovation Center of Advanced Microstructures
School of Electronic Science and Engineering
Nanjing University
Nanjing 210093, China

Recent levels of interest in topological semimetals (TSMs) have stimulated a fruitful avenue of research in materials science. Multiple topological nontrivial TSMs have been studied, including Dirac semimetals (DSMs),[1–4] Weyl semimetals (WSMs),[5–9] nodal-line semimetals,[10,11] and Lorentz invariance-breaking type-II WSMs.[12–15] The concept of broken Lorentz invariance also results in a new system termed type-II DSM, in which the Dirac cones are tilted significantly along specific momentum directions,[16–23] leading to a modulated effective mass and the potential for new applications.[24–27] In particular, intrinsic topological superconductivity (TSC)[28–33] could be induced in type-II DSMs due to a finite density of states around the Dirac points, potentially hosting Majorana modes[28–37] with possible applications in topological quantum computations.[38,39]

Materials made of type-II DSMs have been recently discovered in the 1T-$PtSe_2$ family, i.e., $PtSe_2$, $PtTe_2$, and $PdTe_2$.[16,18–21] These materials are group-10 transition-metal dichalcogenides (TMDC), with crystal structures belonging to the $P\bar{3}m1$ space group, offering similar electronic structures consisting of type-II Dirac dispersions protected by C_{3v} symmetry.[16,17] However, these materials are limited by the problem that the Dirac points are far below the Fermi level, and there are several trivial bands crossing the Fermi surface,[16–21] which constrains the use of these materials in transport studies and for future applications. Because the Dirac dispersion in the $PtSe_2$ family is protected by crystal symmetry and the two bands forming the Dirac cone are mainly determined by the p-orbitals of chalcogen,[16,17] substitution of group-9 transition metals, e.g., iridium, for Pt/Pd and forming 1T-$IrTe_2$, may maintain the Dirac dispersion while pulling the Dirac points closer to the Fermi surface. However, as is the case for some TMDCs, 1T-$IrTe_2$ is metastable and a charge density wave (CDW) transition to a monoclinic structure occurs at low temperatures.[40–45] Consequently, the Dirac dispersion does not survive in $IrTe_2$.

Here, we report that Pt doping in $IrTe_2$ not only stabilizes the metastable 1T-phase but also tunes the Fermi level to the Dirac points. As demonstrated by angle-resolved photoemission spectroscopy (ARPES) and first-principle calculations, appropriately tuning the Pt doping concentration can cause the type-II Dirac points to approach the Fermi level. In addition, all the

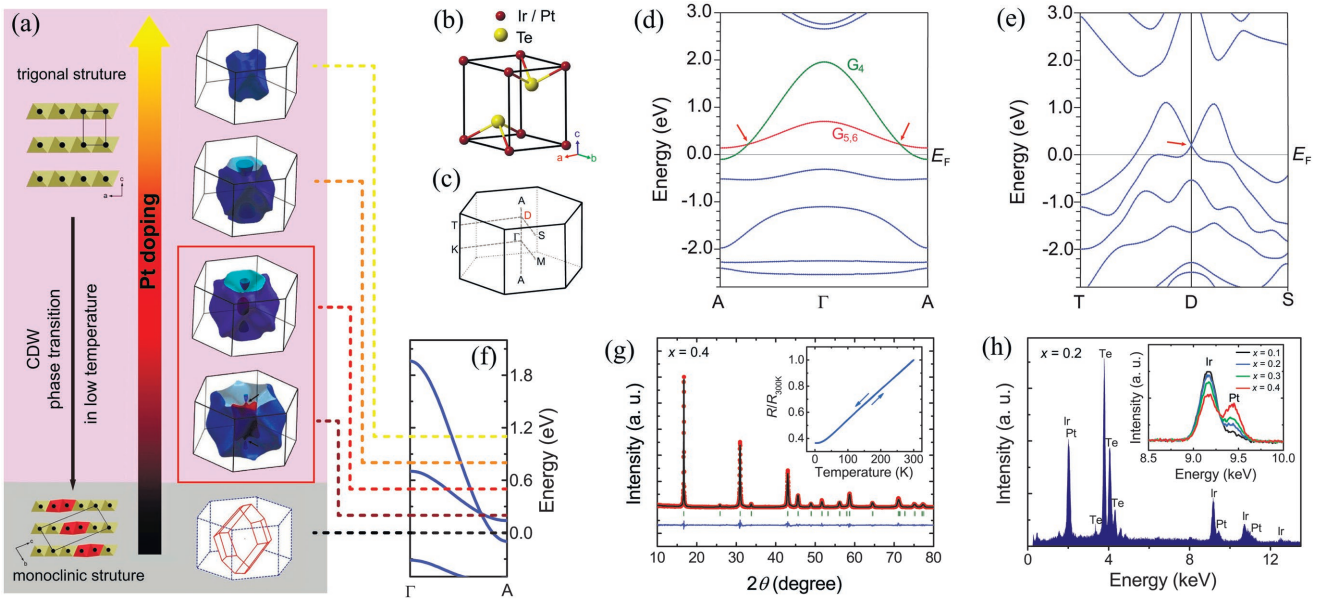

Figure 1. The strategy of platinum doping in 1T-$IrTe_2$ and the characterization of crystals. a) A sketch showing our strategy of platinum doping in 1T-$IrTe_2$. The left-hand panel displays the trigonal crystal structure of 1T- $IrTe_2$. When Pt doping is low, a CDW transition occurs (displayed in gray shade). The right-hand panel in purple shade displays the Fermi surface evolution for various Pt doping of $IrTe_2$, the corresponding Fermi level is indicated by colored dashed line in Figure 2f. b,c) The crystal structure and the Brillouin zone of 1T-$IrTe_2$, respectively. d,e) The band calculation of 1T-$IrTe_2$. f) A zoomed-in view of the tilted Dirac cone along Γ-A. g) The powder XRD pattern of $Ir_{0.6}Pt_{0.4}Te_2$. The blue curve shows the deviation curve. Green rods display the Bragg-peak positions. The inset is the *R*–*T* curve of the corresponding sample. h) The EDS spectrum of $Ir_{0.8}Pt_{0.2}Te_2$. The inset shows the part of the EDS spectra for samples with $x = 0.1$–0.4.

irrelevant bands are far from the Fermi surface. Interestingly, superconductivity is observed in samples where the Fermi level varies across the Dirac points. This offers an opportunity to investigate phase transitions between topological and trivial superconductors in the presence of time-reversal symmetry, along with the associated Majorana physics.

Our strategy is depicted in **Figure 1**a. When the doping ratio is low, a CDW phase transition occurs at low temperature. The trigonal crystal changes to a monoclinic structure, and the Brillouin zone (BZ) also changes (gray shaded zone). The alteration of the crystal structure also kills the Dirac dispersions. The purple shaded zone indicates the suppression of CDW, and the 1T phase is stabilized when the Pt doping strength increases. Additionally, substituted Pt dopants can introduce carriers and modulate the Fermi level to approach the Dirac point in $Ir_{1-x}Pt_xTe_2$, because there is one more valence electron in platinum than in iridium (shown in the right-hand panel of Figure 1a). Pt doping is thus a way to 'kill two birds with one stone', resulting in an ideal type-II DSM in $Ir_{1-x}Pt_xTe_2$.

To validate our strategy, we first calculated the band structure of pristine 1T-$IrTe_2$ using first-principle calculations. The crystal structure and BZ are displayed in Figure 1b,c. Figure 1d,e shows the dispersions along the A-Γ-A and T-D-S directions. Two bands cross the Fermi level, forming a band-crossing feature along the Γ-A direction (shown by the red arrows). These two bands belong to different representations (G_4 and $G_{5,6}$ respectively); the spin-orbital coupling (SOC) cannot open a gap at the crossing point, and instead a gapless Dirac cone with linear dispersion is formed. This is determined by the C_{3v} symmetry in the system with time-reversal and inversion symmetry.[16,17,46] It is clear from Figure 1d,e that the Dirac cone is untilted in the k_x–k_y plane (T-D-S), but tilts strongly along k_z (A-Γ-A), which is a characteristic of type-II Dirac fermions. Figure 1f shows a magnified view of the tilted Dirac cone. According to our calculations, the Dirac point in 1T-$IrTe_2$ is 200 meV higher than the Fermi level (black dashed line), and much closer to it than for $PtSe_2$ family.[17] The Fermi level can be further adjusted by Pt doping, and the Dirac point will be aligned with the Fermi level in samples for a specific doping strength. Fermi surface evolution through adjustment of the Pt doping is demonstrated in the right-hand panel in Figure 1a (the colored dashed lines indicate the corresponding Fermi level in Figure 1f). The crimson dashed line indicates the Fermi pockets when the Fermi level aligns with the Dirac point. Characteristically for type-II Dirac dispersion, a pair of hole-like and electron-like pockets is formed. The hole-like pocket (in red) is located at the center of the BZ, and the shape of the electron-like pocket is complex and divided into two parts by the boundary of the BZ. The outer part is lantern-shaped and traverses the BZ along the k_z direction, while the inner part is ellipse-shaped and touches the hole-like pocket at the Dirac points (indicated by the black arrows). For samples with a higher Pt doping, the Fermi level is beyond the Dirac point and the pair of hole/electron-like pockets separates from the Dirac points. The hole-like pocket shrinks and finally vanishes with increasing Fermi level, and the two parts of the electron-like pocket combine to form one single pocket in the BZ, as displayed in the top of the right-hand panels in Figure 1a. We note that for the wide range of Fermi-level shifting discussed here (0–1.1 eV), all the pockets are formed by the bands

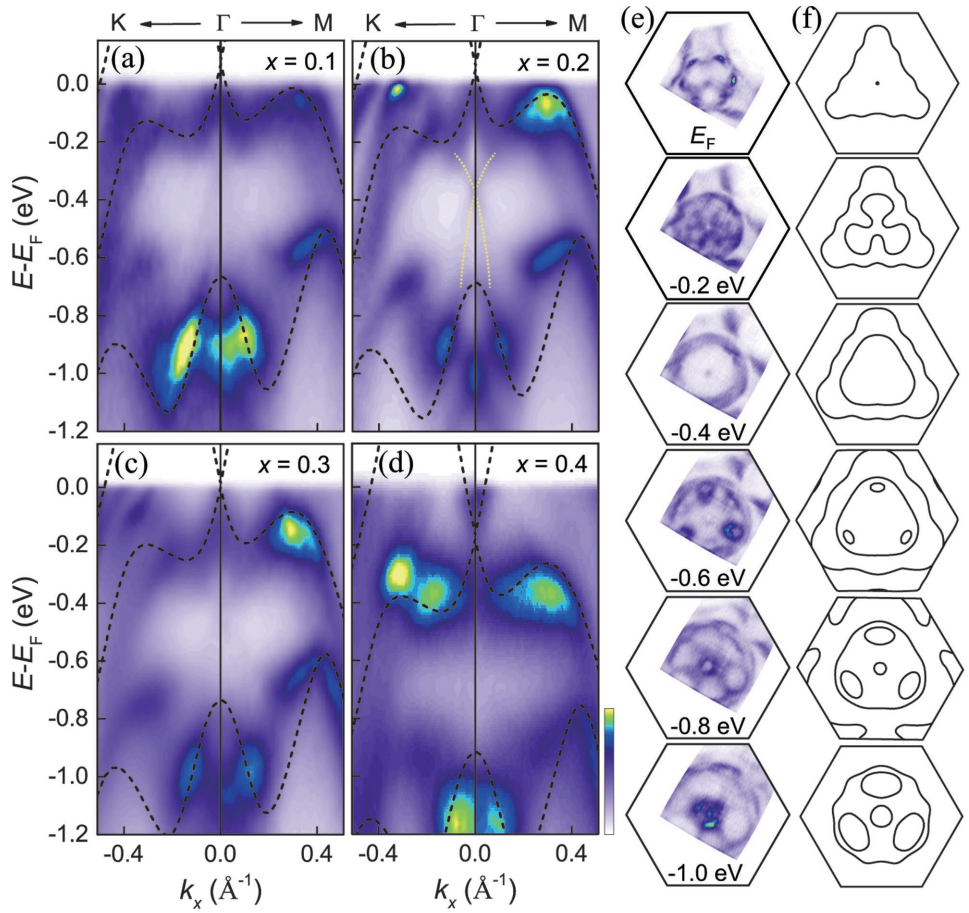

Figure 2. ARPES results for samples with various amounts of doping. a–d) The band dispersions along K-Γ-M of $Ir_{1-x}Pt_xTe_2$ with x = 0.1–0.4. The black dashed lines show the band calculation of $IrTe_2$ (the Fermi energy is shifted to match the experiment). e) Constant energy mappings of the x = 0.2 sample measured from $E - E_F$ = 0 eV to −1 eV. f) Corresponding theoretical calculation (after Fermi energy shifting).

discussed above, and all other irrelevant bands are far from the Fermi surface.

The theoretical analysis described above provides a blueprint for our experiments. The control of the Pt doping strength is crucial not only for the stability of the 1T phase but also for the energy distance from the Dirac point to the Fermi level. We focus on those samples enclosed by the red square in Figure 1a in the following experiments. Single crystals of $Ir_{1-x}Pt_xTe_2$ were grown using the self-flux method. Figure 1g shows the powder X-ray diffraction (XRD) data of one typical $Ir_{1-x}Pt_xTe_2$ sample. (Figure S1a,b in the Supporting Information displays the XRD results for the other samples.) A crystal model with the $P\bar{3}m1$ space group is used to fit to the experimental data. The fitting curve (black line) is consistent with the experimental data (red dots), indicating the pure 1T phase of our samples at room temperature. As discussed above, a CDW phase transition can occur when the temperature decreases. It is therefore necessary to check whether the 1T phase survives at low temperature. The inset in Figure 1g shows resistance against temperature for the corresponding sample. The cooling and heating curves perfectly overlap with no sudden jumps, indicating the absence of any crystal phase transition. Similar results were achieved in other samples with x = 0.1–0.4 (Figure S1c, Supporting Information). Combined with XRD, the stability of the 1T-phase in our samples is confirmed. Figure 1h shows the energy dispersive spectrum (EDS) of one typical sample, and the inset shows part of the spectra corresponding to the La peaks of Ir and Pt from samples with different x. The height of the peaks is normalized using the peaks from Te at around 4 keV. The ratio of the two elements evolves clearly, indicating the successful control of the substituting Pt doping in $Ir_{1-x}Pt_xTe_2$. The actual atomic ratios of these samples are detected by electron probe microanalyzer and the detailed result can be seen in the Supporting Information.

After confirming the crystal structure and elemental composition, we performed ARPES measurements to detect the band dispersions in the $Ir_{1-x}Pt_xTe_2$. **Figure 2**a–d shows the dispersions along the K-Γ-M direction of $Ir_{1-x}Pt_xTe_2$ for x = 0.1–0.4. The black dashed lines show the band calculations for $IrTe_2$. The Fermi energy obtained by calculation is shifted in each panel and the calculations are qualitatively consistent with the experimental data. The offset of the Fermi level in the different samples is clear. For the samples with x = 0.1 and x = 0.2, the Dirac point is a little higher than the Fermi level (≈0.08 eV for x = 0.1; ≈0.05 eV for x = 0.2). For the sample with x = 0.3, the Dirac point is aligned with the Fermi level. For the sample with

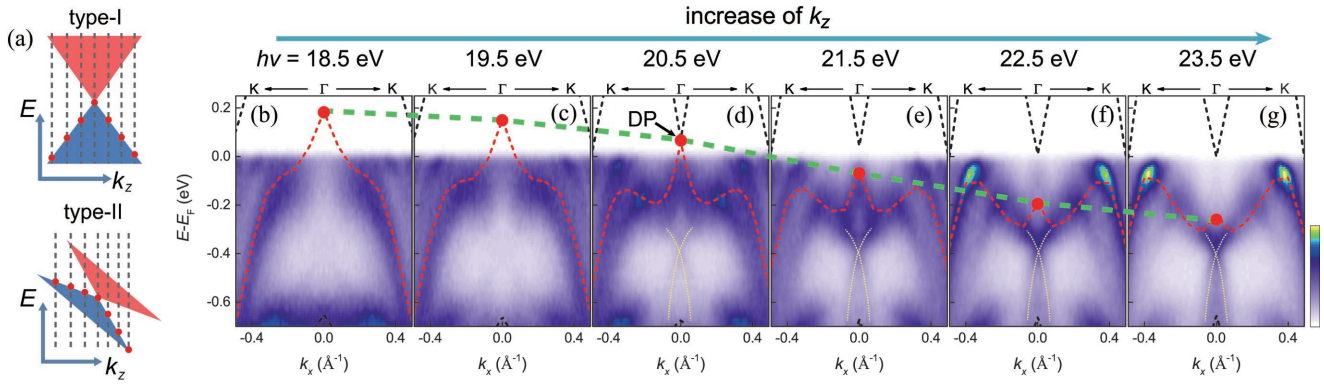

Figure 3. Type-II Dirac property in $Ir_{1-x}Pt_xTe_2$. a) A sketch of type-I and type-II Dirac cones. b–g) Dispersions of $Ir_{0.8}Pt_{0.2}Te_2$ measured at photon energies from 18.5 to 23.5 eV. The red dashed lines show the calculation of the valence band forming Dirac cone. The red dots mark the top position of the valence band at Γ point and the evolution of the top position under various photon energies is indicated by the green dashed lines. The arrow in panel d marks the position of the Dirac point (DP).

x = 0.4, the Dirac point is about 0.2 eV lower than the Fermi level, and the upper part of the Dirac cone can be detected by ARPES. We also measured the constant energy contours of our samples. Figure 2e shows the constant energy mappings of the sample for x = 0.2, measured from the Fermi level to 1 eV less than the Fermi energy. The corresponding theoretical calculations of $IrTe_2$ after the Fermi energy shift are displayed in Figure 2f and are in good agreement with the experimental results. The constant energy mappings of other samples were also obtained as shown in Figure S2 in the Supporting Information. Clear k_z projection can be found in dispersions detected along Γ-K as the bands forming the Dirac cone show significant changes along this direction under various photon energies. In Figure 2b, a cross-like feature can be seen, marked by the yellow dotted lines (also in Figure 2a, c and d but obscured). We believe this to be a surface Dirac cone state, consistent with previous reports.[16,47]

To reveal the bulk properties of the Dirac cone in $Ir_{1-x}Pt_xTe_2$, we used various photon energies to collect the k_z dispersions. **Figure 3**b–g show the dispersions along the G-K direction of the sample with x = 0.2 measured at photon energies from 18.5 to 23.5 eV. The band calculations at the corresponding k_z momentum are also plotted, as shown by the black and red dashed lines. The k_z values are calculated with an inner potential of 13 eV. The evolution of the Dirac cone dispersion can clearly be seen, revealing its bulk properties, while the surface Dirac cone dispersions (indicated by the yellow dotted lines) remain constant except for the changing intensity. In addition, the type-II properties of the Dirac cone can also be revealed, and a sketch showing the type-I and type-II Dirac cones is shown in Figure 3a. The top positions of the valence band (the Γ point in our case) under different momentum (k_z in our case) are indicated by the red dots. For a type-I Dirac cone, the top position is highest at the Dirac point. However, for a tilted type-II Dirac cone, the top position changes monotonically when the momentum sweeps over the region of the cone. As seen in our data, the valence band forming the Dirac cone is marked by the red dashed lines, and the position at the Γ point is marked by the red dot in each panel. It is clear that when the photon energy is low (18.5 and 19.5 eV), the top position of the valence band is somewhat higher than the Fermi level. When increasing the photon energy, i.e., increasing k_z, the position at the Γ point gradually reduces as shown by the green dashed line in Figure 3b–g, which fits well with the type-II case.

After verifying the type-II Dirac dispersion and the Fermi level tunability in $Ir_{1-x}Pt_xTe_2$, we then investigated the electrical transport properties. There are several previous reports of superconductivity in $Ir_{1-x}Pt_xTe_2$[41,43,45]; in these cases, however, the Pt doping level was far lower than it was in our samples. We measured the transport of our samples at ultra-low temperature using a dilution refrigerator and found that the superconductivity survived in $Ir_{1-x}Pt_xTe_2$ for a wide range of x values. As shown in the curves of resistance versus temperature shown in **Figure 4**a, for the sample with x = 0.1, the superconducting critical temperature (T_C) is around 1.7 K, which is consistent with a previous report.[41] When the Pt doping strength is increased, T_C gradually decreases and T_C = 0.65 K for the sample with x = 0.2. When the doping level is further increased to x = 0.3, the superconductivity remains but T_C drops to just 0.15 K. The superconductivity finally disappears in the samples with x = 0.4 in the observable range of temperature (>50 mK). A phase diagram summarizing our results is shown in Figure 4b. When x < 0.04, a CDW transition occurs at low temperature.[41] By increasing the Pt doping, the 1T-phase is stabilized, and there is an emergence of superconductivity. The critical temperature decreases when the doping level is further increased from x = 0.1–0.3 and the superconductivity finally disappears when x = 0.4. By further considering the relationship between the Dirac point and the Fermi energy for the corresponding samples obtained by ARPES (as sketched in Figure 4c), we note that the Dirac points in the samples exhibiting superconductivity are close to the Fermi level. Superconductivity even survives in the sample in which the Fermi level is aligned with the Dirac point (x = 0.3). It is well known that in conventional type-I DSMs there is a low bulk density of states (DOS) near the Dirac point, which prohibits intrinsic superconductivity from occurring when the Fermi level approaches the Dirac points. However, the tilted Dirac dispersions in type-II DSMs lead to a pair of electron and hole pockets, and a finite DOS is always present near the Dirac point[12,17] (the calculated DOS of different Pt-doped $Ir_{1-x}Pt_xTe_2$ samples can be seen in Figure S3 in the Supporting Information). Thus

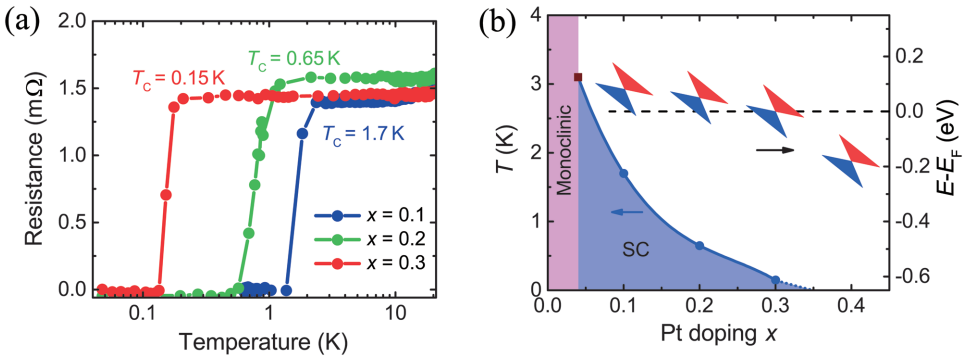

Figure 4. Superconductivity of $Ir_{1-x}Pt_xTe_2$ samples. a) Resistance versus temperature of samples with $x = 0.1$–0.3. b) The superconductivity phase diagram of $Ir_{1-x}Pt_xTe_2$. The brown data point of $x = 0.04$ is cited from ref. [41]. The sketch displays the relative relationship between Fermi level (black dashed line) and Dirac points in the corresponding samples.

superconductivity could be promoted in type-II DSMs. More interestingly, the coexisting electron and hole bulk Fermi surfaces are highly asymmetric with respect to the Dirac point energy in type-II DSMs, and if TSC could be induced in such a system, taking account of the interplay between the bulk and nontrivial surface states near the Dirac points, an exotic topological phase transition could occur in the bulk superconductors when the Fermi level is tuned across the Dirac points (a detailed discussion can be found in the Supporting Information).

In summary, the material $Ir_{1-x}Pt_xTe_2$, is an interesting platform combining the type-II Dirac cone, Fermi level tunability, and superconductivity, enabling further studies on the exotic transport properties of type-II Dirac semimetals, such as quantum oscillation with a nontrivial Berry phase, anisotropic magneto-transport, and Klein tunneling in momentum space.[24] In addition, the potential applications of type-II DSMs such as Dirac materials catalysis[27] may be expected and investigated in $Ir_{1-x}Pt_xTe_2$. Superconductivity in this material may also open a new route to the future investigation of possible TSC and Majorana physics.

Experimental Section

Crystal Growth: Single crystals of $Ir_{1-x}Pt_xTe_2$ with different x values were grown using the self-flux method. A set amount of iridium powder (99.9%, aladdin), platinum sponge (99.98%, Alfa Aesar), and tellurium shot (99.99%, aladdin) with an atomic ratio of $0.18(1-x):0.18x:0.82$ were placed in an alumina crucible. The crucible was vacuum-sealed in a thick-walled ampoule. The ampoule was heated and kept at 950 °C for 10 h, then at 1160 °C for 24 h. The melt was then slowly cooled to 880 °C over a week. The Te flux was then separated from the products by centrifugation.

Angle-Resolved Photoemission Spectroscopy: ARPES measurements were performed at BL13U of the Hefei National Synchrotron Radiation Laboratory. The samples were cleaved in situ and measured in the chamber at a pressure below 10^{-10} Torr.

Theoretical Calculations: Electronic structure calculations were carried out using the full potential linearized augmented plane-wave method as implemented in the WIEN2K package.[48] The General Gradient Approximate for the correlation potential was used. We also used the second-order variational procedure to include the SOC interaction. The lattice constants were $a = b = 3.93$ Å and $c = 5.39$ Å taking a space group of $P\bar{3}ml$. The muffin-tin radii for Ir and Te were set to 1.32 and 1.27 Å, respectively. The basic functions were expanded to $R_{mt}K_{max} = 7$ (where R_{mt} is the smallest of the muffin-tin sphere radii and K_{max} is the largest reciprocal lattice vector used in the plane-wave expansion). A $14 \times 14 \times 9$ k-point mesh was used for the Brillouin zone integral. The self-consistent calculations were considered to converge when the difference in the total energy of the crystal did not exceed 0.1 mRy.

Supporting Information

Supporting Information is available from the Wiley Online Library or from the author.

Acknowledgements

F.C.F. and X.Y.B. contributed equally to this work. The authors gratefully acknowledge the financial support of the National Key R&D Program of China (2017YFA0303203), the National Key Projects for Basic Research of China (2013CB922103), the National Natural Science Foundation of China (91421109, 91622115, 11522432, 61176088, 11274003, U1732273 and U1732159), the Natural Science Foundation of Jiangsu Province (BK20160659 and BK20130054), the Fundamental Research Funds for the Central Universities, and the opening Project of the Wuhan National High Magnetic Field Center. The authors also thank Professor Mark A. Reed from Yale University for stimulating discussions.

Conflict of Interest

The authors declare no conflict of interest.

Keywords

ARPES, Dirac semimetals, superconductors, topological materials, type-II

[1] T. Liang, Q. Gibson, M. N. Ali, M. Liu, R. J. Cava, N. P. Ong, *Nat. Mater.* **2015**, *14*, 280.
[2] Z. K. Liu, J. Jiang, B. Zhou, Z. J. Wang, Y. Zhang, H. M. Weng, D. Prabhakaran, S. K. Mo, H. Peng, P. Dudin, T. Kim, M. Hoesch,

Z. Fang, X. Dai, Z. X. Shen, D. L. Feng, Z. Hussain, Y. L. Chen, *Nat. Mater.* **2014**, *13*, 677.
[3] S.-Y. Xu, C. Liu, S. K. Kushwaha, R. Sankar, J. W. Krizan, I. Belopolski, M. Neupane, G. Bian, N. Alidoust, T.-R. Chang, H.-T. Jeng, C.-Y. Huang, W.-F. Tsai, H. Lin, P. P. Shibayev, F.-C. Chou, R. J. Cava, M. Z. Hasan, *Science* **2015**, *347*, 294.
[4] Z. K. Liu, B. Zhou, Y. Zhang, Z. J. Wang, H. M. Weng, D. Prabhakaran, S.-K. Mo, Z. X. Shen, Z. Fang, X. Dai, Z. Hussain, Y. L. Chen, *Science* **2014**, *343*, 864.
[5] X. Wan, A. M. Turner, A. Vishwanath, S. Y. Savrasov, *Phys. Rev. B* **2011**, *83*, 205101.
[6] H. M. Weng, C. Fang, Z. Fang, B. A. Bernevig, X. Dai, *Phys. Rev. X* **2015**, *5*, 011029.
[7] L. X. Yang, Z. K. Liu, Y. Sun, H. Peng, H. F. Yang, T. Zhang, B. Zhou, Y. Zhang, Y. F. Guo, M. Rahn, D. Prabhakaran, Z. Hussain, S. K. Mo, C. Felser, B. Yan, Y. L. Chen, *Nat. Phys.* **2015**, *11*, 728.
[8] S.-Y. Xu, I. Belopolski, N. Alidoust, M. Neupane, G. Bian, C. Zhang, R. Sankar, G. Chang, Z. Yuan, C.-C. Lee, S.-M. Huang, H. Zheng, J. Ma, D. S. Sanchez, B. Wang, A. Bansil, F. Chou, P. P. Shibayev, H. Lin, S. Jia, M. Z. Hasan, *Science* **2015**, *349*, 613.
[9] S.-M. Huang, S.-Y. Xu, I. Belopolski, C.-C. Lee, G. Chang, B. Wang, N. Alidoust, G. Bian, M. Neupane, C. Zhang, S. Jia, A. Bansil, H. Lin, M. Z. Hasan, *Nat. Commun.* **2015**, *6*, 7373.
[10] J. Hu, Z. Tang, J. Liu, X. Liu, Y. Zhu, D. Graf, K. Myhro, S. Tran, C. N. Lau, J. Wei, Z. Mao, *Phys. Rev. Lett.* **2016**, *117*, 016602.
[11] S. Pezzini, M. R. van Delft, L. M. Schoop, B. V. Lotsch, A. Carrington, M. I. Katsnelson, N. E. Hussey, S. Wiedmann, *Nat. Phys.* **2018**, *14*, 178.
[12] A. A. Soluyanov, D. Gresch, Z. Wang, Q. Wu, M. Troyer, X. Dai, B. A. Bernevig, *Nature* **2015**, *527*, 495.
[13] Z. Wang, D. Gresch, A. A. Soluyanov, W. Xie, S. Kushwaha, X. Dai, M. Troyer, R. J. Cava, B. A. Bernevig, *Phys. Rev. Lett.* **2016**, *117*, 056805.
[14] S.-Y. Xu, N. Alidoust*, G. Chang, H. Lu, B. Singh, I. Belopolski, D. S. Sanchez, X. Zhang, G. Bian, H. Zheng, M.-A. Husanu, Y. Bian, S.-M. Huang, C.-H. Hsu, T.-R. Chang, H.-T. Jeng, A. Bansil, T. Neupert, V. N. Strocov, H. Lin, S. Jia, M. Z. Hasan, *Sci. Adv.* **2017**, *3*, e1603266.
[15] I. Belopolski, D. S. Sanchez, Y. Ishida, X. Pan, P. Yu, S. Y. Xu, G. Chang, T. R. Chang, H. Zheng, N. Alidoust, G. Bian, M. Neupane, S. M. Huang, C. C. Lee, Y. Song, H. Bu, G. Wang, S. Li, G. Eda, H. T. Jeng, T. Kondo, H. Lin, Z. Liu, F. Song, S. Shin, M. Z. Hasan, *Nat. Commun.* **2016**, *7*, 13643.
[16] M. S. Bahramy, O. J. Clark, B.-J. Yang, J. Feng, L. Bawden, J. M. Riley, I. Marković, F. Mazzola, V. Sunko, D. Biswas, S. P. Cooil, M. Jorge, J. W. Wells, M. Leandersson, T. Balasubramanian, J. Fujii, I. Vobornik, J. Rault, T. K. Kim, M. Hoesch, K. Okawa, M. Asakawa, T. Sasagawa, T. Eknapakul, W. Meevasana, P. D. C. King, *Nat. Mater.* **2018**, *17*, 21.
[17] H. Huang, S. Zhou, W. Duan, *Phys. Rev. B* **2016**, *94*, 121117(R).
[18] F. Fei, X. Bo, R. Wang, B. Wu, J. Jiang, D. Fu, M. Gao, H. Zheng, Y. Chen, X. Wang, H. B. Song, X. Wan, B. Wang, G. Wang, *Phys. Rev. B* **2017**, *96*, 041201(R).
[19] M. Yan, H. Huang, K. Zhang, E. Wang, W. Yao, K. Deng, G. Wan, H. Zhang, M. Arita, H. Yang, Z. Sun, H. Yao, Y. Wu, S. Fan, W. Duan, S. Zhou, *Nat. Commun.* **2017**, *8*, 257.
[20] H.-J. Noh, J. Jeong, E.-J. Cho, K. Kim, B. I. Min, B.-G. Park, *Phys. Rev. Lett.* **2017**, *119*, 016401.
[21] K. Zhang, M. Yan, H. Zhang, H. Huang, M. Arita, Z. Sun, W. Duan, Y. Wu, S. Zhou, *Phys. Rev. B* **2017**, *96*, 125102.
[22] T. R. Chang, S. Y. Xu, D. S. Sanchez, W. F. Tsai, S. M. Huang, G. Chang, C. H. Hsu, G. Bian, I. Belopolski, Z. M. Yu, S. A. Yang, T. Neupert, H. T. Jeng, H. Lin, M. Z. Hasan, *Phys. Rev. Lett.* **2017**, *119*, 026404.
[23] P.-J. Guo, H.-C. Yang, K. Liu, Z.-Y. Lu, *Phys. Rev. B* **2017**, *95*, 155112.
[24] T. E. O'Brien, M. Diez, C. W. Beenakker, *Phys. Rev. Lett.* **2016**, *116*, 236401.
[25] J. Xiong, S. K. Kushwaha, T. Liang, J. W. Krizan, M. Hirschberger, W. Wang, R. J. Cava, N. P. Ong, *Science* **2015**, *350*, 413.
[26] M. Udagawa, E. J. Bergholtz, *Phys. Rev. Lett.* **2016**, *117*, 086401.
[27] A. Politano, G. Chiarello, C.-N. Kuo, C. S. Lue, R. Edla, P. Torelli, V. Pellegrini, D. W. Boukhvalov, *Adv. Funct. Mater.* **2018**, 1706504.
[28] X. L. Qi, T. L. Hughes, S. Raghu, S. C. Zhang, *Phys. Rev. Lett.* **2009**, *102*, 187001.
[29] L. Fu, C. L. Kane, *Phys. Rev. Lett.* **2008**, *100*, 096407.
[30] J. J. He, T. K. Ng, P. A. Lee, K. T. Law, *Phys. Rev. Lett.* **2014**, *112*, 037001.
[31] X.-L. Qi, T. L. Hughes, S.-C. Zhang, *Phys. Rev. B* **2010**, *82*, 184516.
[32] X.-L. Qi, S.-C. Zhang, *Rev. Mod. Phys.* **2011**, *83*, 1057.
[33] S. Kobayashi, M. Sato, *Phys. Rev. Lett.* **2015**, *115*, 187001.
[34] M.-X. Wang, C. Liu, J.-P. Xu, F. Yang, L. Miao, M.-Y. Yao, C. L. Gao, C. Shen, X. Ma, X. Chen, Z.-A. Xu, Y. Liu, S.-C. Zhang, D. Qian, J.-F. Jia, Q.-K. Xue, *Science* **2012**, *336*, 52.
[35] G. Du, J. Shao, X. Yang, Z. Du, D. Fang, J. Wang, K. Ran, J. Wen, C. Zhang, H. Yang, Y. Zhang, H.-H. Wen, *Nat. Commun.* **2017**, *8*, 14466.
[36] S.-Y. Xu, N. Alidoust, I. Belopolski, A. Richardella, C. Liu, M. Neupane, G. Bian, S.-H. Huang, R. Sankar, C. Fang, B. Dellabetta, W. Dai, Q. Li, M. J. Gilbert, F. Chou, N. Samarth, M. Z. Hasan, *Nat. Phys.* **2014**, *10*, 943.
[37] J. Shen, W.-Y. He, N. F. Q. Yuan, Z. Huang, C.-w. Cho, S. H. Lee, Y. S. Hor, K. T. Law, R. Lortz, *npj Quantum Mater.* **2017**, *2*, 59.
[38] J. Alicea, Y. Oreg, G. Refael, F. von Oppen, M. P. A. Fisher, *Nat. Phys.* **2011**, *7*, 412.
[39] C. Nayak, S. H. Simon, A. Stern, M. Freedman, S. Das Sarma, *Rev. Mod. Phys.* **2008**, *80*, 1083.
[40] M. J. Eom, K. Kim, Y. J. Jo, J. J. Yang, E. S. Choi, B. I. Min, J. H. Park, S. W. Cheong, J. S. Kim, *Phys. Rev. Lett.* **2014**, *113*, 266406.
[41] S. Pyon, K. Kudo, M. Nohara, *Phys. C* **2013**, *494*, 80.
[42] T. Toriyama, M. Kobori, T. Konishi, Y. Ohta, K. Sugimoto, J. Kim, A. Fujiwara, S. Pyon, K. Kudo, M. Nohara, *J. Phys. Soc. Jpn.* **2014**, *83*, 033701.
[43] A. F. Fang, G. Xu, T. Dong, P. Zheng, N. L. Wang, *Sci. Rep.* **2013**, *3*, 1153.
[44] T. Mochiku, Y. Matsushita, A. Sato, Y. Fujisawa, K. Igarashi, T. Machida, H. Sakata, K. Hirata, *Phys. Procedia* **2014**, *58*, 90.
[45] J. J. Yang, Y. J. Choi, Y. S. Oh, A. Hogan, Y. Horibe, K. Kim, B. I. Min, S. W. Cheong, *Phys. Rev. Lett.* **2012**, *108*, 116402.
[46] B. J. Yang, N. Nagaosa, *Nat. Commun.* **2014**, *5*, 4898.
[47] W.-D. Kong, H. Miao, T. Qian, Z.-J. Wang, G. Xu, A.-F. Fang, Y.-B. Huang, P. Zhang, X. Shi, Z. Fang, X. Dai, P. Richard, N.-L. Wang, H. Ding, *Chin. Phys. Lett.* **2015**, *32*, 077402.
[48] P. Blaha, K. Schwarz, G. Madsen, D. Kvasnicka, J. Luitz, *WIEN2K, An Augmented Plane Wave+ Local Orbitals Program for Calculating Crystal Properties*, Karlheinz Schwarz, Technische Universitat Wien, Austria **2001**.